Motion instabilities in tethered buoy WECs

J. Orszaghova*, H. Wolgamot*, S. Draper* and A. Rafiee†
*Oceans Graduate School,
University of Western Australia, 35 Stirling Highway, Crawley, WA 6009, Australia
E-mail: jana.orszaghova@uwa.edu.au, hugh.wolgamot@uwa.edu.au, scott.draper@uwa.edu.au
†Carnegie Clean Energy Ltd, 21 Barker Street, Belmont, WA 6104, Australia
E-mail: arafiee@carnegiece.com

***Abstract*—Theoretical and experimental investigation of yaw motion instability in a submerged axi-symmetric wave energy converter is presented. The device is a truncated vertical cylinder which is taut-moored via three tethers. Assuming linear hydrodynamics, but retaining non-linear geometry associated with the tethers, governing equations are derived in 6 degrees of freedom.**

Due to the axi-symmetry of the system, there is no hydrodynamic excitation moment in yaw. However, the yaw governing equation - correct to second order in buoy motions - reveals a time-varying restoring moment coefficient. Such systems can undergo large oscillations given a small initial perturbation, through the well known Mathieu instability. Targeted regular wave experiments were used to verify the model predictions on the onset of yaw motion instability in the first two instability branches. The yaw motion in a three-tethered system is analogous to sway motion in a single-tethered device. The yaw instability and the transverse/sway motion instability both arise due to coupling with heave. Due to small damping, the instabilities can be prevalent. The theoretical analysis presented is applicable to other floating WECs.

***Index Terms*—submerged buoy WEC, Mathieu instability, yaw instability, mode coupling, parametric resonance**

I. Introduction

Motion instabilities in floating wave energy converters (WECs) have recently been studied by a number of authors. [1] study a pitching device, called SEAREV, which is found to be prone to parametric roll and yaw motion under specific wave conditions. Parametric roll and pitch are examined by [2] for an axi-symmetric heaving device called Wavebob, and by [3] for a floating axi-symmetric oscillating water column. Wave-activated WECs free to move in multiple degrees of freedom may be particularly prone to instabilities as they are designed to undergo large-amplitude motions. In the above studies the motion instabilities in WECs were undesirable as they appeared to be associated with reduction of the productive mode of motion.

Carnegie Clean Energy is developing the CETO technology which consists of a large disc-shaped buoy, which is shallowly submerged. The latest generation of CETO utilises three integrated mooring and PTOs; the buoy is attached to anchoring points on the sea bed via three tethers (see Figure 1). The device can move in six degrees of freedom, and power is extracted from heave, surge and pitch. Due to the axi-symmetry of the device, power can be effectively absorbed from the incident waves irrespective of the angle of incidence. Compared to a single-tethered converter, power absorption can be significantly increased when the other modes of motion (surge and pitch) are coupled to the PTO (see [4] and [5]).

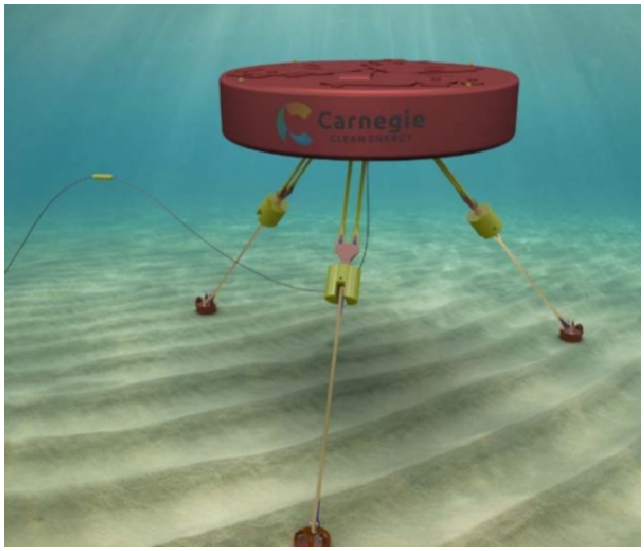

Fig. 1. Diagram of prototype multi-moored CETO wave energy converter with three integrated mooring and PTO systems.

For a single-tethered submerged buoy a mechanism responsible for sway (transverse) motion instability was identified (see [6] and [7]). A time-varying spring coefficient in the sway governing equation arises due to coupling with heave. As such the governing equation can be rewritten as the Mathieu equation, which can give rise to unstable (exponentially growing) solutions given a small perturbation. The simple model based on the Mathieu equation was used to predict onset of instability, and its validity was demonstrated in both regular and irregular tests from previous laboratory campaigns.

Theoretical analysis in this paper reveals that yaw motion in a three-tethered system is analogous to the sway motion in a single-tethered system in a number of ways; the motions do not couple to the power take-off (PTO) at first order, are weakly damped, and are coupled with heave at second order. Mathieu-type instability in yaw motion in a three-tethered system is thus investigated with targeted regular wave experiments.

II. Model Derivation

Let us define a fixed coordinate system centred at the initial position of the buoy's centre of gravity (CoG), with horizontal

axes x and y and vertical axis z, with the incident waves assumed to propagate along the x-axis. Let $\boldsymbol{X} = [X\ Y\ Z]^{\mathrm{T}}$ be the buoy's CoG translational motions of surge, sway and heave along the fixed coordinate system axes. Let $\boldsymbol{\theta} = [\theta_x\ \theta_y\ \theta_z]^{\mathrm{T}}$ denote the buoy's rotational motions about a translating coordinate system, which is centred at the instantaneous CoG and whose axes are parallel to the fixed coordinate system. These extrinsic rotations are referred to as roll, pitch and yaw respectively. Aspects of the derivation that follows are analogous to the work of [7] and [5]. Figure 2 shows a diagram of the buoy under consideration. The centre of buoyancy is assumed to coincide with the CoG. The derivation below assumes a symmetric arrangement of equal length tethers, with one tether pointing in the down-wave direction (along the positive x axis), and two tethers pointing obliquely up-wave. The tether attachment points on the buoy's hull are denoted by position vectors $\boldsymbol{A}_i$ with $i = 1 \ldots 3$. The anchor points on the sea bed are denoted by position vectors $\boldsymbol{S}_i$ with $i = 1 \ldots 3$. Their definitions are

$$
\begin{aligned}
\boldsymbol{A}_1 &= \boldsymbol{X} + \boldsymbol{R}\,[r\mathrm{s}_\theta, 0, -r\mathrm{c}_\theta]^{\mathrm{T}}, \\
\boldsymbol{A}_2 &= \boldsymbol{X} + \boldsymbol{R}\,[-\frac{1}{2}r\mathrm{s}_\theta, -\frac{\sqrt{3}}{2}r\mathrm{s}_\theta, -r\mathrm{c}_\theta]^{\mathrm{T}}, \\
\boldsymbol{A}_3 &= \boldsymbol{X} + \boldsymbol{R}\,[-\frac{1}{2}r\mathrm{s}_\theta, \frac{\sqrt{3}}{2}r\mathrm{s}_\theta, -r\mathrm{c}_\theta]^{\mathrm{T}}, \\
\boldsymbol{S}_1 &= [L\mathrm{s}_\alpha + r\mathrm{s}_\theta, 0, -L\mathrm{c}_\alpha - r\mathrm{c}_\theta]^{\mathrm{T}}, \\
\boldsymbol{S}_2 &= [-\frac{1}{2}(L\mathrm{s}_\alpha + r\mathrm{s}_\theta), -\frac{\sqrt{3}}{2}(L\mathrm{s}_\alpha + r\mathrm{s}_\theta), -L\mathrm{c}_\alpha - r\mathrm{c}_\theta]^{\mathrm{T}}, \\
\boldsymbol{S}_3 &= [-\frac{1}{2}(L\mathrm{s}_\alpha + r\mathrm{s}_\theta), \frac{\sqrt{3}}{2}(L\mathrm{s}_\alpha + r\mathrm{s}_\theta), -L\mathrm{c}_\alpha - r\mathrm{c}_\theta]^{\mathrm{T}},
\end{aligned}
\tag{1}
$$

where s_α, c_α, s_θ and c_θ denote $\sin\alpha$, $\cos\alpha$, $\sin\theta$ and $\cos\theta$ respectively. $\boldsymbol{R}$ is the standard 3x3 rotation matrix (a function of θ_x, θ_y and θ_z; and given in Equation 2), r and θ are respectively the length and the angle (measured from the vertical) of a line between the buoy's centre of gravity and any of the attachment points, and similarly L and α are respectively the length and the angle (measured from the vertical) of the initial/static tethers (when $\boldsymbol{X} = \boldsymbol{\theta} = \boldsymbol{0}$). The superscript $^{\mathrm{T}}$ denotes vector transpose. The rotation matrix is defined as

$$
\boldsymbol{R} = \begin{pmatrix}
\mathrm{c}_y\mathrm{c}_z & -\mathrm{c}_y\mathrm{s}_z & \mathrm{s}_y \\
\mathrm{c}_x\mathrm{s}_z + \mathrm{c}_z\mathrm{s}_y\mathrm{s}_x & \mathrm{c}_x\mathrm{c}_z - \mathrm{s}_y\mathrm{s}_x\mathrm{s}_z & -\mathrm{c}_y\mathrm{s}_x \\
\mathrm{s}_x\mathrm{s}_z - \mathrm{c}_x\mathrm{c}_z\mathrm{s}_y & \mathrm{c}_z\mathrm{s}_x + \mathrm{c}_x\mathrm{s}_y\mathrm{s}_z & \mathrm{c}_y\mathrm{c}_x
\end{pmatrix}, \tag{2}
$$

where s_x and c_x denote $\sin\theta_x$ and $\cos\theta_x$ respectively, and similarly for the pitch θ_y and yaw θ_z.

The instantaneous tether vectors, from the attachment point $\boldsymbol{A}_i$ to the anchor point $\boldsymbol{S}_i$, are given by $\boldsymbol{T}_i = \boldsymbol{S}_i - \boldsymbol{A}_i$. PTO extension ΔL_i and PTO velocity $\Delta\dot{L}_i$, which represent the change in tether length and the rate of change of the tether length respectively, are thus defined as

$$
\begin{aligned}
\Delta L_i &= |\boldsymbol{T}_i| - L, \\
\Delta\dot{L}_i &= \frac{\partial}{\partial t}|\boldsymbol{T}_i|,
\end{aligned}
\tag{3}
$$

where $|\ .\ |$ represents the magnitude of the vector under consideration (i.e. the Euclidean norm). When allowing for motions in all 6 degrees of freedom, the full expressions for PTO extension and PTO velocity are complicated. By setting $\alpha = \theta = 0$, we recover the expressions for a single-tethered device (see [7]).

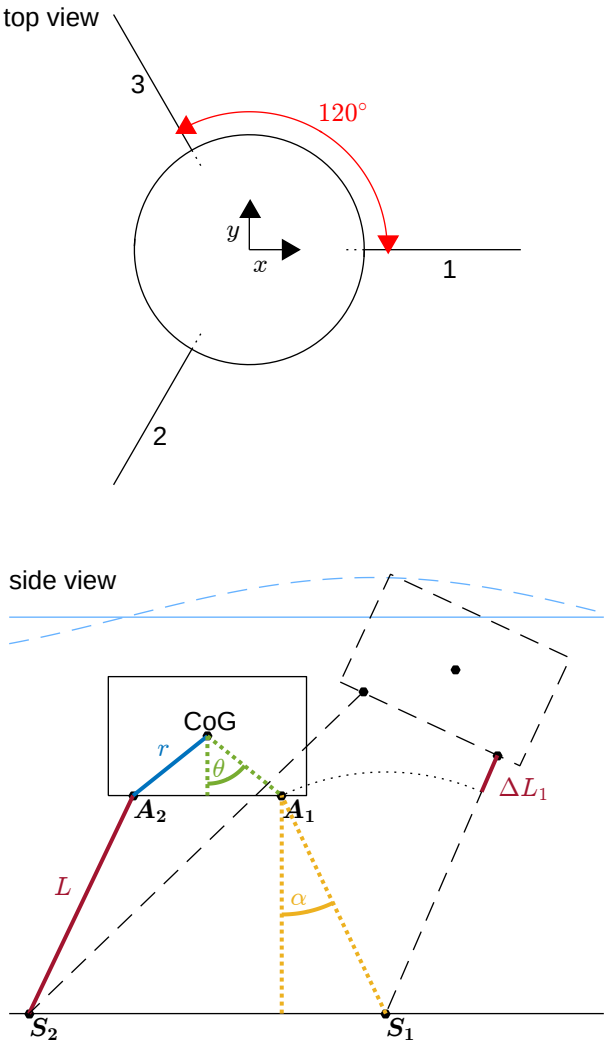

Fig. 2. Schematic diagram of three-tethered CETO converter.

The governing equations, in 6 degrees of freedom, are derived below. The forces considered to be acting on the WEC are buoyancy minus self-weight, hydrodynamic forces and tether forces.

The net buoyancy force $\boldsymbol{F}_B$ acts vertically upwards. For a fully submerged buoy considered here, the expression is independent of the instantaneous body position. When the centre of gravity and the centre of buoyancy coincide, as is assumed here, the buoyancy force moments $\boldsymbol{M}_B$ vanish completely. The expressions read

$$
\begin{aligned}
\boldsymbol{F}_B &= [0, \quad 0, \quad \rho V g - mg]^{\mathrm{T}}, \\
\boldsymbol{M}_B &= [0, \quad 0, \quad 0]^{\mathrm{T}},
\end{aligned}
\tag{4}
$$

where ρ is the fluid density, V and m are the buoy volume and mass, and g is the magnitude of the gravitational acceleration.

The tether, or power take-off, forces $\boldsymbol{F}_{PTOi}$ act along each tether (with $i = 1 \dots 3$). The PTO implementation considered here is composed of a pre-tension force, a linear spring restoring force and a linear damping force. We note that the pre-tension forces counteract the buoyancy force in still/initial conditions. The PTO forces give rise to moments $\boldsymbol{M}_{PTOi}$. The expressions for both are given as

$$\begin{aligned} \boldsymbol{F}_{PTOi} &= \Big(\frac{C}{3\,\cos\alpha} + K\Delta L_i + B\Delta\dot{L}_i\Big)\frac{\boldsymbol{T}_i}{|\boldsymbol{T}_i|}, \\ \boldsymbol{M}_{PTOi} &= \big(\boldsymbol{A}_i - \boldsymbol{X}\big) \times \boldsymbol{F}_{PTOi}, \end{aligned} \tag{5}$$

where C denotes the magnitude of the buoyancy force $C = |\boldsymbol{F}_B| = \rho V g - mg$, K is the linear spring coefficient, B is the linear damping coefficient and $\times$ denotes a vector cross product. The PTO settings, K and B values, are assumed identical for all three tethers. In the PTO force expression, the terms in the brackets represent the tether tension magnitude, which is multiplied by a unit vector of the appropriate orientation to yield the horizontal and vertical force components.

Assuming linear hydrodynamics, the radiation and diffraction problems are decoupled, and the governing equations are given by

$$\boldsymbol{M}\begin{pmatrix}\ddot{\boldsymbol{X}}\\ \ddot{\boldsymbol{\theta}}\end{pmatrix} = \begin{pmatrix}\boldsymbol{F}_B\\ \boldsymbol{M}_B\end{pmatrix} + \begin{pmatrix}\boldsymbol{F}_{PTO}\\ \boldsymbol{M}_{PTO}\end{pmatrix} + \begin{pmatrix}\boldsymbol{F}_{exc}\\ \boldsymbol{M}_{exc}\end{pmatrix} + \begin{pmatrix}\boldsymbol{F}_{rad}\\ \boldsymbol{M}_{rad}\end{pmatrix}, \tag{6}$$

where $\ddot{\boldsymbol{X}}$ and $\ddot{\boldsymbol{\theta}}$ are the buoy's translation and rotation accelerations, and $\boldsymbol{M}$ is the 6x6 mass and moments of inertia matrix, with non-zero entries only along the main diagonal due to the definition of our coordinate system and the buoy shape. The contributions from all three tethers are expressed as $\boldsymbol{F}_{PTO} = \sum_{i=1}^{3}\boldsymbol{F}_{PTOi}$ and $\boldsymbol{M}_{PTO} = \sum_{i=1}^{3}\boldsymbol{M}_{PTOi}$. $\boldsymbol{F}_{exc}$ and $\boldsymbol{M}_{exc}$ are the hydrodynamic excitation forces and moments, which are due to the incident and diffracted waves. $\boldsymbol{F}_{rad}$ and $\boldsymbol{M}_{rad}$ are the radiation forces and moments, which are due to the hydrodynamic pressure resulting from the buoy's motion. As only planar incident waves in the x-direction are considered, and the buoy is assumed cylindrical, $\boldsymbol{F}_{exc}(2) = 0$ and $\boldsymbol{M}_{exc}(1) = \boldsymbol{M}_{exc}(3) = \boldsymbol{M}_{rad}(3) = 0$.

III. LINEARISED MODEL

The governing equations can be linearised, by retaining only first order terms from a multi-variable Taylor expansion of the power take-off forces and moments. The dynamic equations of motion, interpreted in the frequency domain, are given in Equations 7, 8 and 9.

The surge and pitch motions are coupled, both hydrodynamically and through the tether. The coupled governing equations for sway and roll have been omitted for brevity, as they are equivalent to the homogeneous version of Equation 7.

$$\begin{pmatrix} m + a_{11} & a_{15} \\ a_{15} & I_{yy} + a_{55}\end{pmatrix}\begin{pmatrix}\ddot{X}\\ \ddot{\theta}_y\end{pmatrix} + \boldsymbol{B}\begin{pmatrix}\dot{X}\\ \dot{\theta}_y\end{pmatrix} + \boldsymbol{K}\begin{pmatrix}X\\ \theta_y\end{pmatrix} = \begin{pmatrix}\boldsymbol{F}_{exc}(1)\\ \boldsymbol{M}_{exc}(2)\end{pmatrix}, \tag{7}$$

where

$$\boldsymbol{B} = \begin{pmatrix}B_{11} & B_{15}\\ B_{15} & B_{55}\end{pmatrix} \quad \text{and} \quad \boldsymbol{K} = \begin{pmatrix}K_{11} & K_{15}\\ K_{15} & K_{55}\end{pmatrix},$$

such that

$$\begin{aligned} B_{11} &= b_{11} + \frac{3B\mathrm{s}_\alpha^2}{2}, \\ B_{15} &= b_{15} + \frac{3Br}{4}\Big(\mathrm{c}_{2\alpha-\theta} - \mathrm{c}_\theta\Big), \\ B_{55} &= b_{55} + \frac{3Br^2}{2}\mathrm{s}_{\alpha-\theta}^2, \\ K_{11} &= \frac{3K}{2}\mathrm{s}_\alpha^2 + \frac{C}{2L}\Big(\mathrm{c}_\alpha + \frac{1}{\mathrm{c}_\alpha}\Big), \\ K_{15} &= \frac{3Kr}{4}\Big(\mathrm{c}_{2\alpha-\theta} - \mathrm{c}_\theta\Big) - \frac{Cr}{4L\mathrm{c}_\alpha}\Big(3\mathrm{c}_\theta + \mathrm{c}_{2\alpha-\theta}\Big), \\ K_{55} &= \frac{3Kr^2}{4}\Big(1 - \mathrm{c}_{2\alpha-2\theta}\Big) + Cr\Big(\mathrm{c}_\theta + \frac{\mathrm{s}_\alpha}{2\mathrm{c}_\alpha}\mathrm{s}_\theta\Big) \\ &\quad + \frac{Cr^2}{2L}\Big(\frac{1}{\mathrm{c}_\alpha} + \mathrm{c}_{\alpha-2\theta}\Big). \end{aligned}$$

To first order, the heave and yaw motions are uncoupled from the other modes.

$$(m + a_{33})\ddot{Z} + (3B\mathrm{c}_\alpha^2 + b_{33})\dot{Z} + \Big(3K\mathrm{c}_\alpha^2 + \frac{C\mathrm{s}_\alpha^2}{L\mathrm{c}_\alpha}\Big)Z = \boldsymbol{F}_{exc}(3). \tag{8}$$

$$I_{zz}\ddot{\theta}_z + \Big(\frac{Cr^2\mathrm{s}_\theta^2}{L\mathrm{c}_\alpha} + \frac{Cr\mathrm{s}_\alpha\mathrm{s}_\theta}{\mathrm{c}_\alpha}\Big)\theta_z = 0. \tag{9}$$

In the above equations, a_{jk} and b_{jk} denote the frequency-dependent added mass (or added moment of inertia) and radiation damping coefficients respectively, and I_{jj} are the buoy's moments of inertia. The hydrodynamic coefficients for a submerged truncated vertical cylinder are computed according to the analytical solution of [8], [9] and [10]. As the buoy is axi-symmetric, the only linear hydrodynamic cross-mode coupling elements are $a_{15} = a_{51} = -a_{24} = -a_{42}$, and similarly $b_{15} = b_{51} = -b_{24} = -b_{42}$, while also $a_{11} = a_{22}$, $b_{11} = b_{22}$, $a_{44} = a_{55}$, $b_{44} = b_{55}$, $I_{xx} = I_{yy}$, and $a_{66} = b_{66} = 0$.

At first order, all modes of motion, apart from yaw, couple to the PTO and thus contribute to the overall power production. When $\alpha = \theta$, the expressions agree with those presented in [5]. The pitch motion becomes independent of the PTO. The cross-coupling terms in the surge-pitch equations reduce to $B_{15} = b_{15}$ and $K_{15} = \frac{Cr}{L}$, and as such the surge-pitch coupling is weak for a small thin buoy in deep water. When $\alpha = \theta = 0$, the system becomes equivalent to a single-tethered device.

The governing equation for yaw is uncoupled from the other modes. The restoring force is due to buoyancy/pre-tension. In our simplified model, the yaw motion is un-damped. We recall that in a single-tethered system, when $\alpha = \theta = 0$, all non-inertial terms in the linear yaw governing equation vanish, which is clearly not the case here. We would like to draw comparisons between the yaw equation in the three-tethered system and the sway equation in the single-tethered system. For completeness, the (decoupled) sway equation is shown

below (see [7] for derivation, or deduce from Equation 7 by imposing $\alpha = \theta = 0$).

$$(m + a_{22})\ddot{Y} + b_{22}\dot{Y} + \frac{C}{L}Y = 0 \tag{10}$$

We note similarities between Equations 9 and 10:
- the motions do not couple to the PTO,
- there is no exciting force/moment,
- the restoring force/moment is due to buoyancy,
- the motions are weakly damped (or not damped at all).

A. Natural frequencies

Excluding the excitation and damping terms, natural (undamped) angular frequencies $\omega_n = 2\pi f_n$ in the above modes can be easily computed by assuming the variables are time-harmonic.

The yaw natural frequency $\omega_{n6} = 2\pi f_{n6}$ is given by

$$\omega_{n6} = \sqrt{\frac{\frac{Cr^2 \sin^2\theta}{L\cos\alpha} + \frac{Cr\sin\alpha\sin\theta}{\cos\alpha}}{I_{zz}}}. \tag{11}$$

The heave natural frequency $\omega_{n3} = 2\pi f_{n3}$ is given by

$$\omega_{n3} = \sqrt{\frac{3K\cos^2\alpha + \frac{C\sin^2\alpha}{L\cos\alpha}}{m + a_{33}}}. \tag{12}$$

We note that if the heave added mass a_{33} was constant, and not frequency dependent, a single value of the natural frequency ω_{n3} would follow. However, due to frequency dependence of the hydrodynamic coefficient, multiple resonances can arise.

For the coupled surge-pitch (and sway-roll) equations, an eigenvalue problem arises, with the eigenvalues ω_n^2 representing the square of the natural frequencies and the eigenvectors $\boldsymbol{v}_n$ representing the associated mode shapes. The expressions are given below.

$$\begin{aligned} \omega_{n15\pm} &= \sqrt{\frac{-b \pm \sqrt{b^2 - 4ac}}{2a}}, \\ \boldsymbol{v}_{n15\pm} &= \begin{pmatrix} a\omega_{n15\pm}^2 + K_{15}a_{15} - K_{55}(m + a_{11}) \\ -K_{11}a_{15} + K_{15}(m + a_{11}) \end{pmatrix}, \end{aligned} \tag{13}$$

where

$$\begin{aligned} a &= (m + a_{11})(I_{yy} + a_{55}) - a_{15}^2, \\ b &= -(m + a_{11})K_{55} - (I_{yy} + a_{55})K_{11} + 2a_{15}K_{15}, \\ c &= K_{11}K_{55} - K_{15}^2. \end{aligned}$$

Similarly to heave, due to frequency dependence of the hydrodynamic coefficients a_{11}, a_{15} and a_{55}, more than two roots for ω_{n15} are possible.

When $\alpha = \theta$ and the remaining cross-coupling terms $K_{15} = \frac{Cr}{L}$ and a_{15} in Equation 7 are assumed to be small, the expressions for surge and pitch (uncoupled) natural frequencies ω_{n1} and ω_{n5} simplify considerably, as shown below. Lastly, we recall that using this approximation, the pitch motion, and the natural frequency, become decoupled from the PTO.

$$\omega_{n1} \approx \sqrt{\frac{3K\sin^2\alpha + \frac{C}{L}(\cos\alpha + \sec\alpha)}{2(m + a_{11})}} \quad \text{when } \alpha = \theta. \tag{14}$$

$$\omega_{n5} \approx \sqrt{\frac{\frac{Cr(L+r)}{2L}(\cos\alpha + \sec\alpha)}{I_{yy} + a_{55}}} \quad \text{when } \alpha = \theta. \tag{15}$$

The computed natural frequencies are displayed in Figure 3, together with (normalised) experimental motion spectra. The measurements are from irregular wave runs for a buoy with two different mooring arrangements (specified by angle θ, and denoted by θ_{high} and θ_{low}). More details on the experimental campaigns are provided in Section V. We note that for a given buoy geometry, it is not always possible to align the heave and surge-pitch natural frequencies with the incident wave frequencies (by choosing appropriate value of the mechanical stiffness coefficient K). The plots suggest that the computed values for ω_{n6} and ω_{n15-} are reasonably accurate. We recall that the yaw natural frequency is independent of the PTO settings, and simply depends on the system geometry. From Equation 11 it follows that smaller θ angles result in lower ω_{n6}, and this trend is clearly seen in Figure 3.

The surge-pitch unit eigenvectors for the two buoys and the applied PTO settings from Figure 3, calculated according to Equation 13, are $\boldsymbol{v}_{n15-} = [-0.59, \quad 0.81]^T$ and $\boldsymbol{v}_{n15-} = [-0.13, \quad 0.99]^T$. These suggest that at the ω_{n15-} natural frequency, the pitch and surge motions would be out of phase in both runs. For the buoy with θ_{high} both surging and pitching motion would occur (with surge (in m) slightly lower compared to pitch (in radians)), whereas for the buoy with θ_{low} the motion would be highly pitch dominated. The top plots in Figure 4 display the calculated phase difference between surge and pitch motions, from cross-spectral analysis of the experimental measurements. The observed behaviour at ω_{n15-} matches the theoretical prediction. The bottom plots in Figure 4 display components of a unit vector of the experimental surge and pitch motion amplitudes (calculated from the motion spectra in Figure 3). At ω_{n15-} the agreement with the theoretical unit eigenvectors is very satisfactory. We note that as the natural frequency ω_{n15+} is within the incident wave spectrum, the eigen-analysis results would not be reflected in the measurements, and as such are omitted.

In the spectral plots we note presence of yaw motion. Although not discernible from these normalised plots, we note that the yaw rotations could become quite substantial in certain tests. We recall that due to our axi-symmetric geometry, there is no yaw excitation moment, and as such yaw cannot be excited by the fluid alone. In the next Section we therefore extend our model in order to try to explain the experimentally observed yaw oscillations. We note in passing that for the measurements shown, the surge and pitch responses do not coincide with the incident wave frequencies. This non-linearity will not be investigated in this work, however.

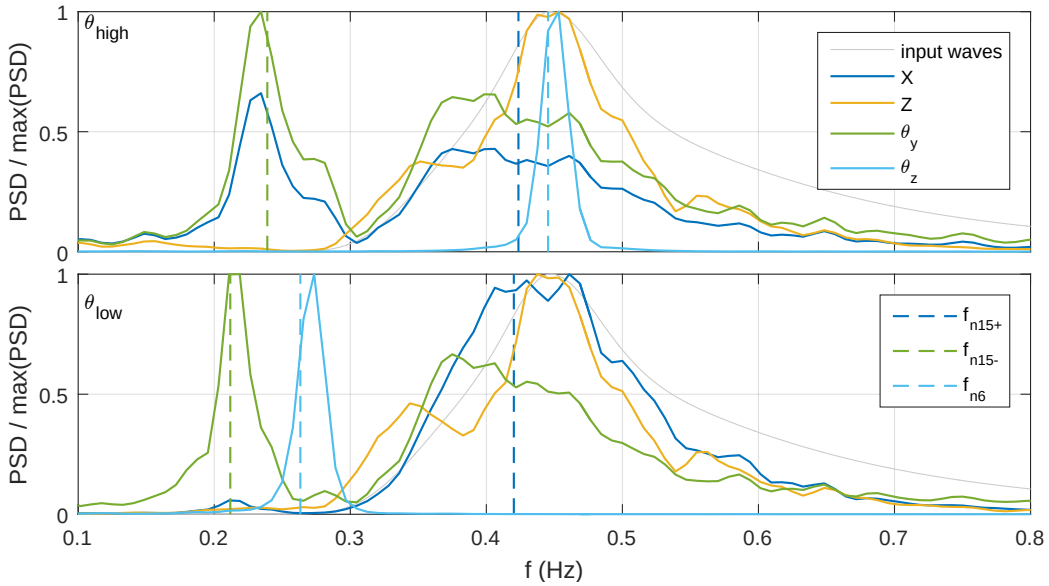

Fig. 3. Wave and response spectra from irregular wave runs, for a buoy with θ_{high} (top plot) and a buoy with θ_{low} (bottom plot). The natural frequencies $f_n = \frac{\omega_n}{2\pi}$ from Equations 11 - 13 are shown by dashed vertical lines.

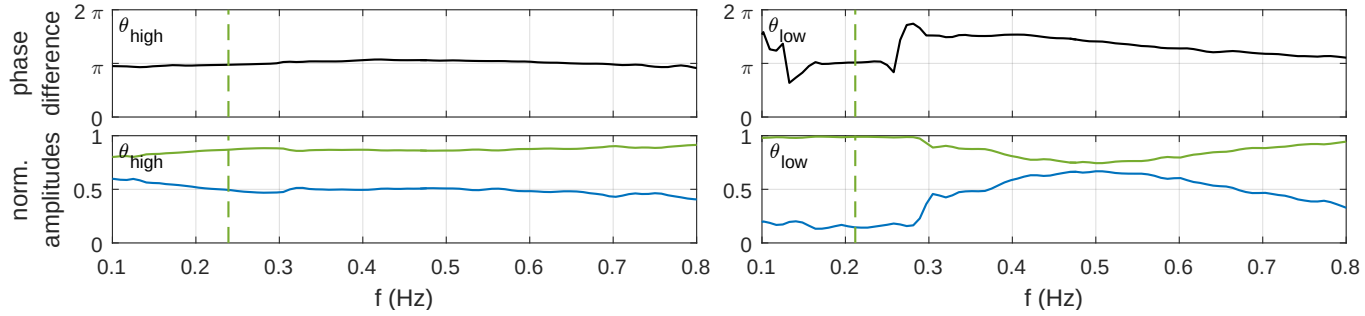

Fig. 4. Phase difference between surge and pitch (top plot) and unit vector of surge (blue) and pitch (green) motion amplitudes (bottom plot) for the runs in Figure 3. The natural frequencies $f_n = \frac{\omega_n}{2\pi}$ from Equations 12 - 15 are shown by vertical lines, and the same legend for these as in Figure 3 applies.

IV. SECOND ORDER MODEL

Retaining terms of up to second order in the buoy motion variables, another set of approximate governing equations can be derived. When allowing for $\alpha \neq \theta$, the expressions are rather lengthy, and will not be given below. In this section, we focus on the second order yaw equation.

Equation 16 is the second order governing equation for yaw in a three-tethered system. The first two terms follow from Equation 9. The third term represents second order coupling between yaw and heave (and yaw and heave velocity). On the right hand side, we have collected all second order terms independent of yaw.

$$I_{zz}\ddot{\theta}_z + \beta\frac{C}{\mathrm{c}_\alpha}\theta_z + \beta\Big((3K\mathrm{c}_\alpha - \frac{C}{L})Z + 3B\mathrm{c}_\alpha\dot{Z}\Big)\theta_z = F, \quad (16)$$

where

$$\beta = \Big(\frac{r^2\mathrm{s}_\theta^2}{L} + r\mathrm{s}_\alpha\mathrm{s}_\theta\Big),$$

$$F = F(X\theta_x, Y\theta_y, \theta_x\theta_y, X\dot{Y}, \dot{X}Y, X\dot{\theta_x}, \dot{X}\theta_x, Y\dot{\theta_y}, \dot{Y}\theta_y, \theta_x\dot{\theta_y}, \dot{\theta_x}\theta_y).$$

In our previous work on a single-tethered buoy, the decoupled sway second order governing equation was derived in [7], and is given below.

$$(m + a_{22})\ddot{Y} + b_{22}\dot{Y} + \frac{C}{L}Y + \Big((\frac{K}{L} - \frac{C}{L^2})Z + \frac{B}{L}\dot{Z}\Big)Y = 0. \quad (17)$$

We note similarities between Equations 16 and 17 as both contain a time-varying spring coefficient due to the coupling with heave (and heave velocity). If we assume the heave motion to be harmonic at the incoming wave frequency ω, then the equations can be re-written as the classical Mathieu equation.

$$\ddot{Y} + 2\mu\dot{Y} + \Big(\delta + 2\epsilon\cos(2\tau)\Big)Y = 0, \quad (18)$$

where the non-dimensionalised time τ is given by $\omega t = 2\tau$, and as such the non-dimensional damping coefficient is 2μ, the non-dimensional spring coefficient is $\delta = 4(\frac{\omega_n}{\omega})^2$, and

the amplitude of the oscillating spring coefficient is 2ϵ. From Equation 16 it follows that

$$\epsilon = \frac{2}{\omega^2}\frac{A_Z}{I_{zz}}\beta\sqrt{\left(3K\mathrm{c}_\alpha - \frac{C}{L}\right)^2 + \omega^2(3B\mathrm{c}_\alpha)^2}, \qquad (19)$$

where A_Z is the harmonic heave motion amplitude. We note that Equation 16 is an undamped version of the Mathieu equation, with a non-zero right hand side. For stability analysis only the homogeneous equation is considered, and as such the additional terms do not preclude us from the same analysis as was pursued in [7]. However, the right hand side terms could be considered as excitation terms which could lead to a perturbation which triggers the instability.

According to Floquet theory, the Mathieu equation admits both bounded and unbounded solutions. Without any external excitation, an initial perturbation can grow exponentially if the system is in the unstable regime. Figure 5 shows the stability diagram for the Mathieu equation. We see that the first two instability branches are most likely to be troublesome, as damping significantly reduces the further instability regions. The first and second instability branches correspond to $\omega = 2\omega_{n6}$ and $\omega = \omega_{n6}$ respectively. Odd-numbered instability branches exhibit a period-doubling phenomenon, meaning that the underlying period of the unstable response/motion is twice the period of the oscillating restoring force/moment component. Even-numbered instability branches do not posses this period-doubling behaviour. We have indicated this in the diagram. We note that in practice the small perturbations will always be present (even in well controlled laboratory experiments, and of course in the ocean). However, the growth of the unstable motion will not be unbounded (as predicted by the Mathieu equation), but eventually saturate at a level dependent on the dissipation in that mode and the full non-linear structure of the governing equations.

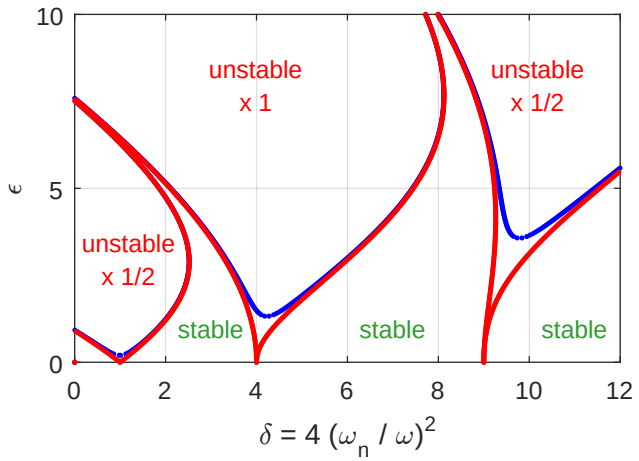

Fig. 5. Stability diagram for the damped (blue curve, $\mu = 0.1$) and undamped (red curve, $\mu = 0$) Mathieu equation.

V. EXPERIMENTAL RESULTS

Results from a model-scale experimental campaign carried out by Carnegie Clean Energy and the University of Western Australia are presented. The experiments were conducted in the Ocean basin at the Coastal, Ocean And Sediment Transport laboratory (COAST lab) at the University of Plymouth, UK. Parameters of the tested model CETO device are listed in Table I. Two different mooring arrangements (characterised by angle θ) were tested, and are referred to as θ_{high} and θ_{low}. Details of the integrated mooring and power take-off system are omitted from the Table for confidentiality reasons.

The free surface elevation at a number of locations around the WEC was measured by wave gauges. A Qualisys motion capturing system was used to track the buoy instantaneous position (in 6 degrees of freedom). Three model scale power take-offs were used, each consisting of a tether, a winch and a pulley. Each pulley was attached to the bottom of the basin, and the tether would pass through it onto the computer-controlled winch, which was positioned above water. The winch torque, as well as the length of the reeled and un-reeled tether were continuously measured. As such a prescribed tension force function (such as the one given below in Equation 6), could be achieved. PTO extension and tether tension were also recorded. A large number of tests, primarily using irregular wave conditions, were carried out, together with a smaller selection of regular wave tests. All tests utilised uni-directional waves.

TABLE I
BUOY PARAMETERS (MODEL SCALE).

parameter	value
buoy radius (m)	0.625
buoy height (m)	0.25
buoy mass m (kg)	249
water depth (m)	1.5
submergence depth (m)	0.1

Targeted regular wave experiments were conducted to check the presence of yaw instability predicted by our simple model. For the buoy with θ_{high}, the calculated yaw natural period is 2.2s (10s in full scale), and as such the second instability branch (where $\omega = \omega_{n6}$) was investigated. The range of incident wave periods was 1.7 - 2.8s (7.5 - 12.5s in full scale). For the buoy with θ_{low} the yaw natural frequency is around 3.8s (17s in full scale). The first instability branch (where $\omega = 2\omega_{n6}$) was investigated, with the range of incident wave periods of 1.5 - 2.7s (7 - 12s in full scale). The intention was to run multiple tests at each frequency, such that tests both above and below the instability boundary would be carried out. By varying the incident wave amplitudes, and thus the resultant heave motion, the vertical position ϵ in the stability diagram changes.

Using the buoy parameters and the applied PTO coefficients (K, B and C values), together with the experimental heave amplitude A_Z, the values of δ and ϵ are evaluated for each test. These are plotted in the stability diagrams in Figure 6. Each run has been colour-coded by examining the recorded yaw motion. Runs which exhibited noticeable yaw oscillations (mean yaw oscillation amplitude threshold set to 1°) are displayed in red. On the other hand, runs with

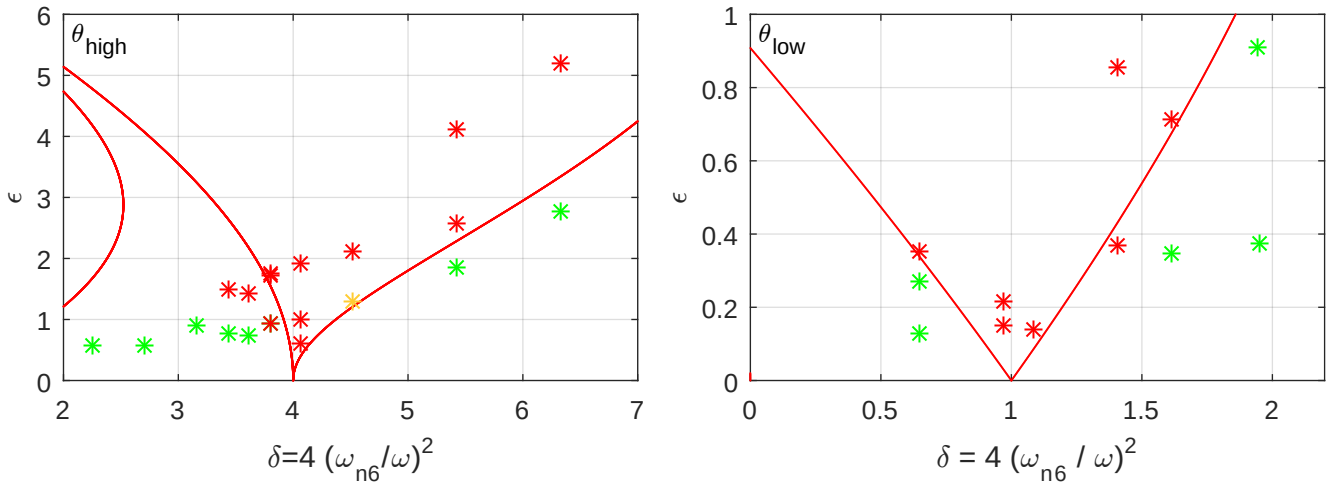

Fig. 6. Regular wave experiments plotted on the stability diagram for the un-damped Mathieu equation. Left: Investigation of the second instability branch (centred at $\omega = \omega_{n6}$) for a buoy with θ_{high}. Right: Investigation of the first instability branch (centred at $\omega = 2\omega_{n6}$) for a buoy with θ_{low}.

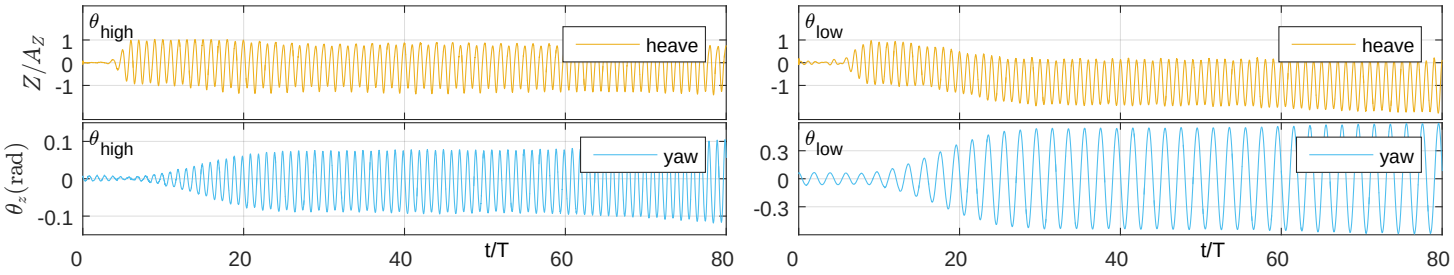

Fig. 7. Timeseries of heave and yaw motion from regular wave experiments. The x-axis has been normalised with the incident wave period T, and the heave motion timeseries has been normalised with the harmonic heave amplitude A_Z . Left: test $[\delta, \epsilon] \approx [4, 1]$ for a buoy with θ_{high}. Right: test $[\delta, \epsilon] \approx [0.97, 0.15]$ for a buoy with θ_{low}.

minimal recorded yaw motion are shown in green. If our model worked flawlessly, all red markers would be above the predicted instability boundaries. The orange marker was used to denote a test in which the buoy exhibited yaw motion initially (oscillations of $\pm 5°$ during the first 30 wave periods), followed by the buoy remaining stable for the remainder of the test ($\approx$ 100 wave periods).

From Figure 6 we note that our instability prediction is reasonably accurate for both buoys. Our model cannot give an indication of the yaw oscillation amplitudes. It simply predicts the onset of the yaw instability. From the measured yaw timeseries we note that for the θ_{high} buoy, the maximum yaw motion recorded in the regular wave runs was within $\pm 20°$, whereas for the θ_{low} buoy, the maximum yaw oscillations could reach $\pm 45°$. This is perhaps not surprising as for a buoy with attachment points $\boldsymbol{A}_i$ closer to its centre (i.e. smaller angle θ), the yaw moments due to the tether force are smaller, and as such provide a weaker restrain.

Figure 7 shows the measured heave and yaw timeseries from two of the regular wave tests. The period doubling phenomenon in yaw is clearly visible in the bottom right plot. This test is for the θ_{low} buoy and corresponds to the middle of the first instability branch where $\omega \approx 2\omega_{n6}$ (i.e. $\delta \approx 1$). Such behaviour is characteristic for odd-numbered instability branches. The recorded yaw motions from the second instability branch do not exhibit period-doubling, the yaw motion is at the incident wave frequency. This can be seen in the left plots in Figure 7, which correspond to a test for the θ_{high} buoy at $\omega \approx \omega_{n6}$ (i.e. $\delta \approx 4$).

VI. CONCLUSIONS AND DISCUSSION

Mathieu-type yaw motion instability was studied, theoretically and experimentally, in an axi-symmetric submerged tethered buoy system with three integrated mooring and PTOs. The governing equations of the WEC in six degrees of freedom were derived taking into account hydrostatic, linear hydrodynamic and PTO forces and moments. Various degrees of non-linearity associated with the tethers were considered. At first order (in buoy motion variables), the natural frequencies in all modes were identified. All modes of motion, apart from yaw, are coupled to the PTO at first order. The yaw natural frequency depends on tether pretension, mass moment of inertia of the buoy and geometrical parameters of the mooring systems.

Similarities between the yaw motion in a three-tethered system and the sway motion in a single-tethered system were highlighted. The motions are not strongly damped, and are

subject to Mathieu-type instability due to a coupling with heave. The occurrence of yaw instability was verified by laboratory experiments with two different mooring arrangements tested. A range of regular wave periods of 7 - 12s (in full scale) was used. The instability prediction from our model was satisfactory. In both mooring set-ups, notable yaw oscillations were observed in tests which fell well within the predicted instability branches. However, some inconsistencies remain, which we hope to resolve by coupled analysis of the other modes of motion. In the present work we considered yaw-heave coupling only, whereas in fact all modes of motion are coupled at second order. Additionally, analysis of yaw motion instability in irregular tests is also remaining.

Implications of the yaw instability in irregular waves, for power absorption and for design of the integrated mooring and PTO system, remain to be identified. If necessary, mitigating strategies may be adopted, thanks to the understanding of the yaw motion instability mechanism identified in this work. Changing the yaw natural frequency such that the incident wave frequencies did not align with at least the first two instability branches would reduce occurrence of the instability. Increased damping in yaw, perhaps in the form of short bilge keels, would also be beneficial, as this would shrink the instability branches.

The analysis presented in this paper aims to enhance understanding of parametrically excited motions in WECs, which is a phenomenon likely to affect many wave-activated WEC designs which are free to respond in a number of modes. In this respect, we would like to highlight the usefulness of laboratory tests. Numerical simulations might disregard modes of motion not directly excited by the fluid (for example sway, roll and yaw for a symmetric device), or might utilise symmetry to only model part of the domain, and as such would not reveal such motions.

ACKNOWLEDGMENT

This research was supported under Australian Research Council's Linkage Project scheme (LP150100598). The laboratory tests performed at the COAST lab Ocean basin at the University of Plymouth, UK were supported by MaRINET2 funding (Project ID 1299). Provision of the experimental data from Carnegie Clean Energy is gratefully acknowledged.

REFERENCES

[1] A. Babarit, H. Mouslim, A. Clément, and P. Laporte-Weywada, "On the numerical modelling of the nonlinear behaviour of a wave energy converter," in *International Conference on Offshore Mechanics and Arctic Engineering, Volume 4: Ocean Engineering; Ocean Renewable Energy; Ocean Space Utilization, Parts A and B*. Honolulu, Hawai: ASME, May-June 2009, pp. 1045–1053. [Online]. Available: http://dx.doi.org/10.1115/OMAE2009-79909

[2] K. Tarrant and C. Meskell, "Investigation on parametrically excited motions of point absorbers in regular waves," *Ocean Engineering*, vol. 111, no. Supplement C, pp. 67–81, 2016. [Online]. Available: http://www.sciencedirect.com/science/article/pii/S0029801815005880

[3] R. P. F. Gomes, J. D. C. M. Ferreira, S. R. e Silva, J. C. C. Henriques, and L. M. C. Gato, "An experimental study on the reduction of the dynamic instability in the oscillating water column spar buoy," in *Proceedings of the 12th European Wave and Tidal Energy Conference (EWTEC)*, Cork, Ireland, August-September 2017.

[4] M. A. Srokosz, "The submerged sphere as an absorber of wave power," *Journal of Fluid Mechanics*, vol. 95, no. 4, pp. 717–741, 1979.

[5] N. Sergiienko, A. Rafiee, B. Cazzolato, B. Ding, and M. Arjomandi, "Feasibility study of the three-tether axisymmetric wave energy converter," *Ocean Engineering*, vol. 150, pp. 221–233, 2018. [Online]. Available: https://www.sciencedirect.com/science/article/pii/S002980181730793X

[6] J. Orszaghova, H. Wolgamot, R. Eatock Taylor, S. Draper, A. Rafiee, and P. H. Taylor, "Simplified dynamics of a moored submerged buoy," in *Proceedings of the 32nd International Workshop on Water Waves and Floating Bodies (IWWWFB)*, Dalian, China, April 2017.

[7] J. Orszaghova, H. Wolgamot, R. Eatock Taylor, P. H. Taylor, and A. Rafiee, "Transverse motion instability of a submerged moored buoy," *Proceedings of the Royal Society A*, Submitted.

[8] G. McCauley, H. Wolgamot, J. Orszaghova, and S. Draper, "Linear hydrodynamic modelling of arrays of submerged oscillating cylinders," *Submitted to Applied Ocean Research*, Submitted.

[9] S.-C. Jiang, Y. Gou, B. Teng, and D.-Z. Ning, "Analytical solution of a wave diffraction problem on a submerged cylinder," *Journal of Engineering Mechanics*, vol. 140, no. 1, pp. 225–232, 2014. [Online]. Available: https://ascelibrary.org/doi/abs/10.1061/\%28ASCE\%29EM.1943-7889.0000637

[10] S.-C. Jiang, Y. Gou, and B. Teng, "Water wave radiation problem by a submerged cylinder," *Journal of Engineering Mechanics*, vol. 140, no. 5, p. 06014003, 2014. [Online]. Available: https://ascelibrary.org/doi/abs/10.1061/\%28ASCE\%29EM.1943-7889.0000723